JOURNAL OF PROPULSION AND POWER
Vol. 26, No. 3, May–June 2010

Direct Numerical Simulation of Transitional and Turbulent Flow on a Turbine Airfoil

Man Mohan Rai*
NASA Ames Research Center, Moffett Field, California 94035

DOI: 10.2514/1.46296

A direct numerical simulation of transitional/turbulent flow on a low-speed turbine airfoil is presented here. The nonconservative form of the Navier–Stokes equations for compressible flows is used for this simulation. The numerical method used to solve these equations is a high-order-accurate upwind-biased iterative-implicit finite-difference scheme and is also presented here. The algorithm and the simulation are extensions of earlier efforts in direct simulations of transition and turbulence on flat plates. The present investigation has additional features, such as surface curvature, an adverse pressure gradient region on the airfoil, and trailing-edge vortex shedding. The results provided in the paper include the time-averaged pressure and the Stanton number distribution on the airfoil surface and turbulence statistics and flow visualization in the transitional/turbulent regions. Comparisons with experimental and computational data obtained for flows over flat plates and in channels are provided. The results indicate that the essential features of transition and turbulence have been captured.

Introduction

CURRENTLY, most of the computational fluid dynamics analyses of propulsion-related flows are performed with the Reynolds-averaged Navier–Stokes (RANS) equations. On occasion, large eddy simulations (LES) are used to more accurately capture the underlying physics. The effects of transition and turbulence are modeled in both these approaches. These model-based computational techniques yield approximations to the true flow physics. Direct numerical simulations (DNS) of transition and turbulence, wherein all the relevant scales are computed, have been limited to simple geometries and low to moderate Reynolds numbers. Direct simulations of transitional/turbulent flows require grids that provide accurate resolution of the smaller scales (typically about 15 to 25 times the Kolmogorov length scale in turbulent flow) while simultaneously encompassing the entire computational region. In high Reynolds number flows the smaller scales are significantly smaller than the largest scales and the computational region. This disparity in scales necessitates large grids and, consequently, large computational resources.

There are many complex phenomena in flow through turbomachinery that require DNS in order to truly capture the underlying physics. Rotor–stator interaction with the attendant turbulent wake–blade interaction and vortex shedding at trailing edges of blades in rotating machinery are just a couple of flow phenomena that require a nonmodeling approach. They contribute to the acoustics and unsteady heat transfer and loads on the machine and can have a significant effect on reliability, safety, and maintenance costs. Direct simulations of such flows are required for both analysis and assessment of advanced designs that address efficiency, safety, and lifetime costs. Fortunately, there are two mitigating factors. First, the Reynolds numbers encountered in rotating machinery are moderate (typically less than 2.0×10^6, based on blade chord) and much smaller when compared with those found in external flows. Second, currently available computational resources are sufficient to perform direct simulations of some of the simpler problems encountered in flow through turbomachinery.

There has been some work in the last few years in performing DNS of turbomachinery airfoil sections. These efforts primarily deal with blade rows from low-pressure turbines (LPTs), for which the flow on the suction side of the airfoil is largely transitional in nature because of the low Reynolds numbers involved. The flow on the pressure side continues to be a subject of research. Here, we review the most relevant ones. In [1], simulated wakes (obtained from a DNS of a temporally evolving wake) are used to compute wake–blade interaction in the case of a LPT blade. The Reynolds number for this case is 148,000, based on the axial chord length. The Navier–Stokes equations (incompressible form) are solved on a staggered mesh. The main emphasis of this study is the evolution of the wake as it is travels through the turbine passage and its effect on both the suction and pressure sides of the airfoil. A discussion of the effect of the principal stresses associated with the base flow on the evolution of the wake is provided. It is argued that soon after the wake enters the turbine stage, the wake segment close to the pressure surface is subjected to stretching along its axis and compression perpendicular to this axis. This results in an alignment of the vortical structures in this segment of the wake along the axis of the wake. This process continues, and even intensifies as this portion of the wake travels downstream, because of the accelerating flow on the second half of the pressure side. On the contrary, the central portion of the wake that forms a bowed shape (apex) finds itself in a region where compression occurs along the axis of the wake. Based on earlier work [2] on plane strained wakes and the computed DNS data, Wu and Durbin [1] explain the resulting intensification of turbulence and the enlargement of the region occupied by the bow of the wake. The effect of the highly stretched wake on the pressure surface, the generation of near-surface streamwise vortices, and their effect on the neighboring flow and heat transfer are discussed in detail. The authors assert that the streamwise vortex pairs found adjacent to the pressure surface are not derived from a Gortler instability but are a forced response to the incident wake. Transition on the suction surface via bypass transition mechanisms is also discussed briefly. In [3,4], the LPT airfoil of [1] is used to perform DNS of the associated flow. The incompressible form of the Navier–Stokes equations are solved with a second-order-accurate central difference scheme in conjunction with a three-step Runge–Kutta method for time integration. The emphasis in these studies is the separation on the suction side resulting from a higher angle of attack and lower Reynolds number.

In a more recent effort [5], that is similar to the one of [1] but mimics the experiments of [6,7], the authors report on a DNS of low Reynolds number flow (72,000 based on the chord) past a turbine airfoil with incoming wakes. Here again, as in [1], the wakes are

Presented as Paper 4460 at the AIAA 42nd Joint Propulsion Conference, Sacramento, CA, 9–12 July 2006; received 10 July 2009; revision received 17 November 2009; accepted for publication 19 November 2009.

*Senior Scientist for Computational Sciences, Exploration Technology Directorate. Associate Fellow AIAA.

simulated wakes that are introduced into the computation via appropriate boundary conditions. A second-order-accurate central-finite-volume method is used to solve the incompressible form of the Navier–Stokes equations. A three-stage Runge–Kutta method is used for time integration. The emphasis of this study [5] is airfoil surface heat transfer and the related flow mechanisms. Phase-averaged statistics were found to indicate significant reductions in shape factor and increases in the turbulent shear stress and kinetic energy in the boundary layer on the first half of the suction side of the airfoil because of wake–blade interaction. The effect of the interaction was much less pronounced further downstream on the suction side, where the flow is mildly turbulent at all phases, and on the entire pressure side.

In [8], the method of [1] is used to perform a DNS of flow through a linear compressor cascade. The emphasis here is the study of transition mechanisms on the pressure surface (pressure gradient is adverse for the first 80% of the chord) and the suction surface (pressure gradient is initially favorable up to 20% of the chord, followed by an essentially adverse pressure gradient all the way to the trailing edge). In the presence of a prescribed level of freestream turbulence, the flow was attached on the pressure surface and exhibited laminar separation followed by turbulent reattachment between 60 and 70% chord on the suction side. The transition processes involved on the two surfaces are discussed in detail in [8].

In the present study, the emphasis is on solving the compressible form of the Navier–Stokes equations using a high-order-accurate fully implicit upwind-biased finite-difference method. The natural dissipation of the method removes the requirement of added artificial dissipation, filters, and dealiasing schemes without unduly affecting solution accuracy. The high-order accuracy of the method both reduces the number of grid points required to obtain a given level of solution accuracy and also reduces the amount of dissipation. The implicit nature of the method permits the use of fairly large Courant numbers, thus further reducing computational requirements. Here, we present the high-resolution/high-accuracy method of the solution (including the basic method and boundary conditions). The finite-difference methodology presented here is used in the context of multiple computational zones, which together comprise the computational region. The use of multiple zones greatly simplifies the grid generation process. The present effort includes code development for general geometries and efficient code implementation on parallel computers. An important objective of this study is to determine the computability of turbomachinery flows on currently available, massively parallel computers. The creation of a database for turbulence and transition modeling is also an integral part of this effort.

This research is an extension of work done in the 1990s ([9,10]); the earlier investigations focused on flows associated with simple geometries, such as rectangular channels and flat plates. The current work addresses general geometries and flows in rotating machines. The high-order method and a corresponding computer program are used to perform a DNS of subsonic flow over a turbine airfoil. This airfoil is representative of a stator in a high-pressure turbine (HPT) with a relatively higher-flow Reynolds number than the LPT cases discussed earlier. The corresponding flow exhibits laminar, transitional, and turbulent regions and hence possesses characteristics found in more complex flows. One of the goals of this study is accurately computing transition to turbulence and the turbulent flow downstream. Transition is achieved here via wall blowing and suction. The magnitude of blowing/suction was adjusted, so that transition occurred at the end of the favorable pressure gradient region on the suction side of the airfoil. This corresponds to an experiment described later to a case without grid-generated turbulence. The ability of the high-order-accurate upwind-biased method in computing bypass transition is demonstrated in [10]. Bypass transition is prevalent in turbomachinery flows, because wake-induced transition is usually via the bypass mode because of the high levels of turbulent intensity in the wakes. However, the methodology presented here can also be used effectively to compute other modes of flow transition. An example of the growth of small amplitude disturbances in a flat plate boundary layer, and the excellent agreement of the computed results with linear theory, are also provided in [10]. Obtaining accurate temperature and velocity statistics in the turbulent region downstream of the transition is another goal of the present study. The results presented here for the turbine airfoil include surface pressure and heat transfer, turbulence statistics in the transitional and turbulent regions, as well as the development of the spanwise vorticity field.

In a single-stage low-speed turbine/compressor, interaction effects on the upstream stator are primarily due to the potential effect (caused by the relative motion between stator and rotor airfoils). On the other hand, the downstream rotor is subjected to wake–blade interaction, interaction between the secondary flows of the stator with the rotor and, as in the case of the stator, the potential effect. Wake–blade interaction computations, such as those reported in [1,5], although contributing to our understanding of turbomachinery flows, do not account for the potential effect. A true stage simulation that includes both rotors and stators in a single coupled computation is required to better understand the complexities of turbine and compressor flows. Aspects, such as the interaction of the secondary flows of upstream rows on downstream airfoils and multistage physics, need a coupled rotor–stator approach. The present work represents a first step in developing the numerical methodology and the computer program to compute stator–rotor interaction via DNS.

Numerical Method

The current effort is an extension of an earlier one to use high-order-accurate upwind-biased finite-difference methods to perform DNS of fully developed, incompressible turbulent flow in a channel [9]. The main objective of this earlier investigation was to provide a comprehensive comparison between the results obtained using finite-difference and spectral methods. The computed data, including first- and second-order turbulence statistics, were found to agree well with both experimental data and earlier spectral simulations on a grid with approximately the same number of grid points. The finite-difference method for incompressible flow, developed in [9], uses upwind-biased finite differences and a time-stepping technique based on a partially implicit, fractional step method [11]. One advantage of the method of [9] is that the dissipative nature of the leading truncation error term of the upwind-biased differences used to approximate the convective terms automatically controls aliasing errors. The second advantage is that the method can be easily extended to curvilinear grids.

The method of [9] was then extended to the nonconservative compressible form of the Navier–Stokes equations [10]. This extension was restricted to rectangular grids. The resulting method is fully implicit and uses fifth-order-accurate upwind-biased finite differences for the convective terms and fourth-order-accurate central differences for the viscous terms. A technique to numerically generate freestream disturbances with prescribed length scales and intensity level is also presented in this study. The high-order finite-difference method was used in [10] to compute low-speed transitional/turbulent flow on a flat plate subjected to high levels of freestream turbulence. The computed data agreed with experimental data and showed that the essential features of the bypass transition process were captured.

To briefly describe the method of [10], we consider the unsteady, compressible, nonconservative formulation of the Navier–Stokes equations in three spatial dimensions:

$$Q_t + AQ_x + BQ_y + CQ_z = \frac{1}{\rho}(R_x + S_y + T_z) \tag{1}$$

In Eq. (1), Q is the vector of independent variables:

$$Q = \lfloor \rho \quad u \quad v \quad w \quad p \rfloor^T \tag{2}$$

where ρ is the density, p is the pressure, and u, v, and w are the velocities in the x, y, and z directions, respectively. The matrices A, B, and C are obtained from the matrix D:

$$D = \begin{pmatrix} q & \rho k_1 & \rho k_2 & \rho k_3 & 0 \\ 0 & q & 0 & 0 & k_1/\rho \\ 0 & 0 & q & 0 & k_2/\rho \\ 0 & 0 & 0 & q & k_3/\rho \\ 0 & \gamma p k_1 & \gamma p k_2 & \gamma p k_3 & q \end{pmatrix} \tag{3}$$

where q is defined as $q = uk_1 + vk_2 + wk_3$. The matrix A is obtained from D with $k_1 = 1$, $k_2 = 0$, and $k_3 = 0$; the matrix B is obtained with $k_1 = 0$, $k_2 = 1$, and $k_3 = 0$; and the matrix C is obtained using $k_1 = 0$, $k_2 = 0$, and $k_3 = 1$. The viscous term R_x on the right-hand side (RHS) of Eq. (1) is given by

$$R_x = \begin{pmatrix} 0 \\ [2\mu u_x + \lambda(u_x + v_y + w_z)]_x \\ [\mu(u_y + v_x)]_x \\ [\mu(u_z + w_x)]_x \\ \phi + \rho[\mu(\gamma p/\rho)_x/Pr]_x \end{pmatrix} \tag{4}$$

where Pr is the Prandtl number, μ is the viscosity, γ is the ratio of specific heats, and

$$\begin{aligned} \lambda &= -2\mu/3 \\ \phi &= \rho(\gamma - 1)\{u_x[2\mu u_x + \lambda(u_x + v_y + w_z)] + v_x[\mu(u_y + v_x)] \\ &\quad + w_x[\mu(u_z + w_x)]\} \end{aligned} \tag{5}$$

The viscous terms S_y and T_z are obtained from similar expressions.

The convective terms AQ_x, BQ_y, and CQ_z in Eq. (1) are evaluated, as in [12]. To illustrate the technique, we consider the term AQ_x. The matrix A can be written as

$$A = P\Lambda P^{-1} \tag{6}$$

where P^{-1} is the matrix of the left eigenvectors of A, and Λ is a diagonal matrix containing the eigenvalues of A. The term AQ_x is evaluated as

$$AQ_x = A^+Q_x^- + A^-Q_x^+ \tag{7}$$

where $A^\pm = P\Lambda^\pm P^{-1}$ and Λ^+ and Λ^- are diagonal matrices containing the positive and negative eigenvalues of A, respectively. The terms Q_x^- and Q_x^+ are backward and forward differences of the vector Q, respectively. They are evaluated using fifth-order-accurate backward-biased and forward-biased differences on a seven-point stencil [10] as

$$\begin{aligned} Q_x^- &= \frac{-6Q_{i+2} + 60Q_{i+1} + 40Q_i - 120Q_{i-1} + 30Q_{i-2} - 4Q_{i-3}}{120\Delta x} \\ Q_x^+ &= \frac{4Q_{i+3} - 30Q_{i+2} + 120Q_{i+1} - 40Q_i - 60Q_{i-1} + 6Q_{i-2}}{120\Delta x} \end{aligned} \tag{8}$$

on a grid that is equispaced in the x direction. The remaining convective terms are evaluated similarly. The finite-difference stencils used at grid points near boundaries are smaller and yield correspondingly lower orders of accuracy. A more detailed discussion of this approach can be found in [9,10].

The viscous terms are computed using central differences on a five-point stencil to obtain fourth-order accuracy. To illustrate, we consider the term $[\mu(u_y + v_x)]_x$ in the vector R_x. This term is first expanded as

$$[\mu(u_y + v_x)]_x = \mu_x(u_y + v_x) + \mu(u_{xy} + v_{xx}) \tag{9}$$

Each of the derivatives on the RHS of Eq. (9) is then evaluated using central differences.

The fully implicit finite-difference representation of Eq. (1) at any interior grid point is

$$\begin{aligned} &\frac{3Q^{n+1} - 4Q^n + Q^{n-1}}{2\Delta t} + (A^+Q_x^- + A^-Q_x^+ + B^+Q_y^- + B^-Q_y^+ \\ &\quad + C^+Q_z^- + C^-Q_z^+)^{n+1} = \left[\frac{1}{\rho}(R_x + S_y + T_z)\right]^{n+1} \end{aligned} \tag{10}$$

The three-point stencil used in Eq. (10) to approximate the time derivative Q_t yields second-order accuracy in time. Equation (10) represents a system of nonlinear equations and is solved using a Newton–Raphson-type iterative technique at each time step, as in [13].

The fully implicit upwind-biased method of [10], described previously, is extended here to curvilinear coordinate systems. Adopting a general transformation of the kind

$$\tau = t; \quad \xi = \xi(x, y, z); \quad \eta = \eta(x, y, z); \quad \zeta = \zeta(x, y, z) \tag{11}$$

the governing equations [Eq. (1)] take the form

$$Q_\tau + \bar{A}Q_\xi + \bar{B}Q_\eta + \bar{C}Q_\zeta = \frac{1}{\rho}(R_x + S_y + T_z) \tag{12}$$

where

$$\begin{aligned} \bar{A} &= A\xi_x + B\xi_y + C\xi_z; \qquad \bar{B} = A\eta_x + B\eta_y + C\eta_z \\ \bar{C} &= A\zeta_x + B\zeta_y + C\zeta_z \end{aligned} \tag{13}$$

The derivatives Q_ξ, Q_η, and Q_ζ are computed using fifth-order-accurate forward- and backward-biased differences, as before. The convective term $\bar{A}Q_\xi$ is evaluated as before by splitting [12] the matrix $\bar{A}$:

$$\bar{A}Q_\xi = \bar{A}^+Q_\xi^- + \bar{A}^-Q_\xi^+ \tag{14}$$

The terms $\bar{B}Q_\eta$ and $\bar{C}Q_\zeta$ are treated similarly. Although the convective terms do need to be transformed to implement a physically meaningful matrix splitting and biasing of the required finite differences, there is not a corresponding advantage to transforming the viscous terms, because the associated derivatives are obtained using central differences. Hence, the viscous terms in Eq. (12) appear in their original form as derivatives in the x, y, and z directions. However, their evaluation uses derivatives in the transformed coordinate system. For example, the term u_y in Eq. (9) is obtained from

$$u_y = u_\xi\xi_y + u_\eta\eta_y + u_\zeta\zeta_y \tag{15}$$

In Eq. (15), the derivatives of the flow variables, as well as the transformation metrics, are computed using five-point central difference stencils (fourth-order accuracy). Second derivatives are obtained similarly.

The fully implicit nonlinear equations for curvilinear coordinates can now be written as

$$\begin{aligned} &\frac{3Q^{n+1} - 4Q^n + Q^{n-1}}{2\Delta\tau} + (\bar{A}^+Q_\xi^- + \bar{A}^-Q_\xi^+ + \bar{B}^+Q_\eta^- + \bar{B}^-Q_\eta^+ \\ &\quad + \bar{C}^+Q_\zeta^- + \bar{C}^-Q_\zeta^+)^{n+1} = \left[\frac{1}{\rho}(R_x + S_y + T_z)\right]^{n+1} \end{aligned} \tag{16}$$

The linearization and subsequent approximate factorization of Eq. (16) yields the following iterative-implicit upwind-biased high-order-accurate finite-difference method:

$$\left[\alpha \mathrm{I} + \beta\Delta\tau\left(\frac{\bar{A}^{+}\nabla_{\xi}}{\nabla\xi} + \frac{\bar{A}^{-}\Delta_{\xi}}{\Delta\xi}\right)\right]^{m}\left\{\alpha \mathrm{I} + \beta\Delta\tau\left[\frac{\bar{B}^{+}\nabla_{\eta}}{\nabla\eta} + \frac{\bar{B}^{-}\Delta_{\eta}}{\Delta\eta} - \bar{M}\left(\frac{\Delta_{\eta}}{\Delta\eta} + \frac{\nabla_{\eta}}{\nabla\eta}\right) - \bar{N}\left(\frac{\Delta_{\eta}}{\Delta\eta} - \frac{\nabla_{\eta}}{\nabla\eta}\right)\right]\right\}^{m}\left[\alpha \mathrm{I} + \beta\Delta\tau\left(\frac{\bar{C}^{+}\nabla_{\zeta}}{\nabla\zeta} + \frac{\bar{C}^{-}\Delta_{\zeta}}{\Delta\zeta}\right)\right]^{m}(Q^{m+1} - Q^{m}) = -\Delta\tau\left(\frac{3Q^{m} - 4Q^{n} + Q^{n-1}}{2\Delta\tau}\right) - \Delta\tau(\bar{A}^{+}Q_{\xi}^{-} + \bar{A}^{-}Q_{\xi}^{+} + \bar{B}^{+}Q_{\eta}^{-} + \bar{B}^{-}Q_{\eta}^{+} + \bar{C}^{+}Q_{\zeta}^{-} + \bar{C}^{-}Q_{\zeta}^{+})^{m} + \Delta\tau\left[\frac{1}{\rho}(R_{x} + S_{y} + T_{z})\right]^{m} \tag{17}$$

In Eq. (17), $\alpha = 1.5^{1/3}$, $\beta = 1.5^{-2/3}$, ∇, and Δ are backward- and forward-difference operators, respectively, the matrices $\bar{M}$ and $\bar{N}$ represent the linearization of the first and second derivatives in the wall-normal (η) direction, and m is an iteration index. For the sake of brevity, only the viscous terms in the wall-normal direction (η) have been included on the left-hand side (LHS) of the equation (similar terms can, of course, be included in the ξ and ζ direction as required). Additionally, on the LHS, the convective terms are approximated with first-order-accurate formulations and the viscous terms with second-order-accurate formulations. This does not affect accuracy because of the iterative nature of the scheme. In Eq. (17), Q^{m} is an approximation to Q^{n+1}. When $m = 0$, $Q^{m} = Q^{n}$ and, as Eq. (17) is iterated to convergence at a given time step, $Q^{m} \to Q^{n+1}$, and the LHS tends to zero. Because the LHS of Eq. (17) can be driven to zero at every time step, linearization and factorization errors can be driven to zero during the iteration process. Another advantage of the iterative scheme is that it decouples the computations in a multiple-zone computation while simultaneously maintaining the implicit nature of the method over a time step.

An important limitation of the nonconservative formulation of the Navier–Stokes equations is that it can only be used to compute flows that are free of flow discontinuities. However, it was chosen for this study because the associated high-order-accurate finite-difference method can be extended in a straightforward manner to curvilinear coordinate systems. In discontinuity-free flows, these equations do conserve mass, momentum, and energy to an extent consistent with the order of accuracy of the scheme and the grid resolution provided. For example, in the case of the turbine airfoil computation, presented later in the text, the difference between the inlet and the exit mass flow rates was less than 0.08%.

We note here the work of [14], in which an implicit Newton iterative method, based on compact central differences and filters, is used to solve a number of practical problems via an implicit LES approach. A subgrid scale model is not used in [14]; instead, the filter dissipates the turbulent energy contained in the smaller scales. The Newton iterative approach used in [14] is closely related to the one used here (as reported in [15]). It was originally developed in [13]. The advantages attributed to this approach in [14] were discussed in detail in [10,13]. The filters [14] essentially provide the dissipation that is naturally present in upwind schemes. It should be noted that upwind methods are constructed to provide correct signal propagation for hyperbolic systems.

Multiple-Zone Computational Grid

The computational region is divided into multiple zones to facilitate grid generation and provide adequate grid resolution only where it is required. Figure 1 shows the airfoil cross section and the adjacent zone/grid. The original airfoil used in the experiment [16], on which the current simulation is based, is fully three-dimensional. Only the midspan section of the three-dimensional shape is used to generate a three-dimensional grid of a uniform cross section. The computation is, of course, three dimensional. The multiple two-dimensional grids are uniformly spaced in the spanwise direction.

The grid in the zone adjacent to the airfoil (Fig. 1) is generated algebraically. The grid lines moving away from the airfoil are straight lines and intersect the airfoil surface orthogonally. This feature, in addition to yielding a grid with superior qualities in the region of the transitional/turbulent boundary layer, facilitates the computation of profiles of the turbulence statistics in the wall-normal direction. The grid shown in Fig. 1 is only representative of the computational grid. The actual grid provides high resolution in the wall-tangential direction on the latter two-thirds of the suction side and the entire circular trailing edge; the grid spacing in wall units is $\Delta s_{T}^{+} = 22.75$, where s_{T} is the arc length along the airfoil surface. The wall shear velocity and kinematic viscosity used to normalize Δs_{T} is from the turbulent region (at $x/c = 0.95$ on the suction side, where c is the airfoil axial chord, $c = 5.93$ in.). An estimate of the wall shear velocity, required to generate the initial grid, was obtained from a RANS simulation of the flow over the airfoil. The first grid point off the wall is at $\Delta s_{N} = 0.0002$ in. along the entire airfoil surface, where s_{N} is the distance normal to the airfoil surface. In the turbulent region at $x/c = 0.95$, this resolution corresponds to $\Delta s_{N}^{+} = 0.91$. The spanwise extent of the computational region is 0.512 in., and the resolution obtained in this direction is $\Delta z^{+} = 9.10$. The grid size in the adjacent zone is $1801 \times 61 \times 257$: a total of 28,234,277 grid points.

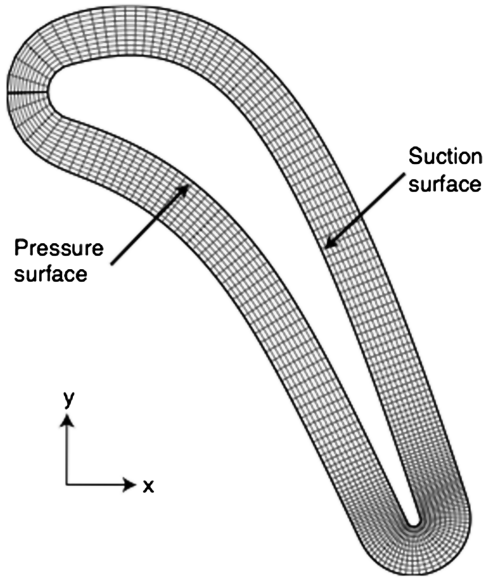

Fig. 1 Midspan airfoil section and representative zone/grid adjacent to the airfoil.

The grid spacing in the wall-tangential direction, on the pressure side of the airfoil, is relatively coarse. This is because the experiment, on which the current computation is based, exhibits laminar flow on the pressure surface (this observation is based on measured Stanton number values). There is no attempt here to perform a direct simulation of the pressure side flow. Additionally, wall-tangential grid resolution in the leading-edge region and the first third of the suction surface is only adequate for computations of laminar flow.

Figure 2 shows the other zones (inlet, exit, and external) and the grid in the external zone. As in the case of the adjacent zone, the external zone is also discretized using an O grid. However, an elliptic grid generator is used to obtain the external grid. The inner boundary of this grid corresponds to a constant η line in the adjacent grid. Similarly, the outer boundary of the adjacent grid corresponds to a constant η line in the external grid. This feature simplifies information transfer between the two grids. The use of the external grid facilitates a reduction in grid resolution in the region away from the wall. The wall-normal extent of the adjacent grid is approximately 4.7 turbulent boundary layer thicknesses ($\delta_{98.5}$ at $x/c = 0.95$ on the suction side) from the airfoil surface. Thus, it provides ample space for the transitional/turbulent boundary layer to evolve on a highly refined grid. The external grid fills a region in which high resolution is not required (unless, of course, airfoil wake evolution is of interest). Thus, the external grid is discretized using a relatively coarse grid with the objective of reducing computational expense.

The constant ξ lines in the external grid, which move away from the airfoil, intersect the inner boundary of this grid orthogonally. The

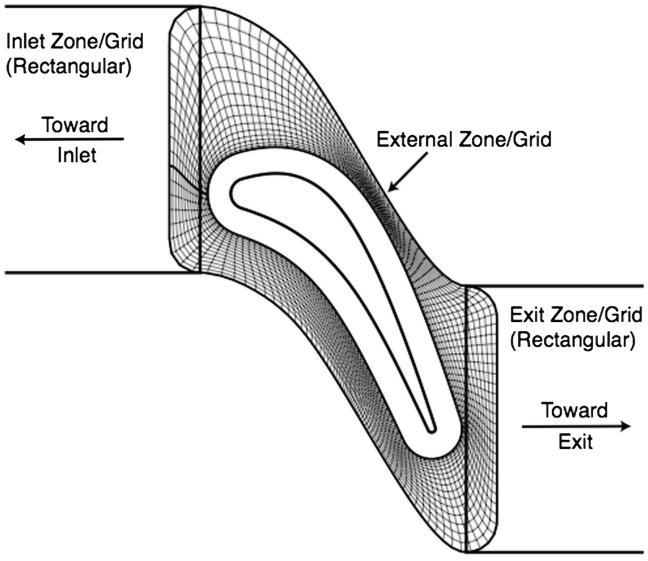

Fig. 2 Multiple zones used to discretize the computational region.

grid spacing in the η direction, at the inner boundary, is the same as the grid spacing in the η direction in the adjacent grid, where the inner boundary of the external grid is located. A portion of the outer boundary of the external grid corresponds to the upper and lower periodic boundary. This periodicity implies an infinite row of airfoils in the y direction. The grid size in the external grid is $301 \times 31 \times 257$: a total of 2,398,067 grid points. Figure 2 also shows portions of the inlet and exit zones. The grid in each of these zones is rectangular. The grid in the inlet zone expands gradually in the x direction as it approaches the inlet boundary. Similarly, the grid in the exit zone expands gradually in the x direction, toward the exit boundary. The overlap between the inlet zone and the external zone permits the transfer of information between these zones. A similar situation exists between the exit zone and the external zone. The grid sizes in the inlet zone and the exit zone are $31 \times 41 \times 257$ and $31 \times 81 \times 257$, respectively. Thus, the total number of grid points used in this simulation is 31,604,318. This system of zonal grids, which is the baseline grid, is referred to as grid B in the rest of the text.

A second, more-refined grid (grid F) with the same general characteristics as the baseline grid was used to perform a grid refinement study. This finer grid has $3301 \times 71 \times 513$ points adjacent to the airfoil and $611 \times 41 \times 513$ points in the external grid. The total number of grid points in grid F is approximately 135 million. The resolution obtained in the well-resolved portion of the airfoil is $\Delta s_T^+ = 11.80$, $\Delta s_N^+ = 0.95$, and $\Delta z^+ = 4.72$, based on the wall shear velocity at $x/c = 0.95$. The grid refinement study of [9], which includes comparisons with both experimental data as well as computed data obtained using a spectral method, indicates that this level of resolution with the order of accuracy used in the present method is adequate to obtain accurate first- and second-order turbulent statistics.

Boundary Conditions

The computational region is discretized using four grids: the adjacent grid, the external grid, and the inlet and exit grids. The boundaries that contain these grids can be broadly classified as natural and zonal boundaries. The natural boundaries include the inlet boundary, the exit boundary, the airfoil surface, the upper and lower periodic boundaries (in Fig. 2), and the boundaries in the spanwise direction. The boundary between the external and adjacent grids is an example of the many zonal boundaries in the computation. Both the natural and zonal boundary conditions used here are similar to those used in [10]. They are presented here to provide continuity for the reader and because some of them are different.

Airfoil Surface Boundary Condition

The heat transfer rate is one of the boundary conditions specified at the airfoil surface. This condition is given by

$$-k_w \partial\theta/\partial s_N = q_w \tag{18}$$

where k_w is the thermal conductivity at the wall, $\partial\theta/\partial s_N$ is the derivative of the temperature in the wall-normal direction at the wall, and q_w is the specified surface heat transfer rate (in the present study, $q_w = 0.139$ Btu/(s · ft^2), as in the experiment of [16]). The other boundary conditions imposed at the surface are a zero normal derivative of the pressure and the no-slip boundary condition. The set of equations used to update the boundary points on the airfoil surface are given next (in these equations, the subscript 1 refers to a grid point on the airfoil surface, the subscript 2 refers to the corresponding grid point just off the surface, and Δs_N is the distance between these points):

$$u_1 = 0; \qquad v_1 = 0; \qquad w_1 = 0; \qquad p_1 = p_2$$
$$\frac{p_1}{\rho_1} = \frac{p_2}{\rho_2} + \frac{q_w \Delta s_N}{k_w} \tag{19}$$

The last two equations assume that the constant ξ grid lines in the adjacent grid intersect the airfoil surface orthogonally. Higher-order-accurate representations of the pressure and temperature derivatives yielded slightly different results in preliminary tests but resulted in more restrictive time steps.

Flow transition was induced via surface blowing and suction upstream of the region in which transition to turbulence was desired. The wall-normal velocity in the blowing/suction strip q_N was obtained from the following equations:

$$q_N = A u_\infty f(T) g(z) h(t); \qquad f(T) = 4\sin(\theta)[1 - \cos(\theta)]/\sqrt{27}$$
$$\theta = 2\pi(T - T_a)(T_b - T_a); \qquad g(z) = \sum_{l=1}^{l_{\max}} Z_l \sin[2\pi l(z/z_{\max} + \phi_l)] \tag{20}$$

with

$$Z_{l+1} = Z_l/1.25$$

and

$$\sum_{l=1}^{l_{\max}} Z_l = 1; \qquad h(t) = \sum_{m=1}^{m_{\max}} T_m \sin[2\pi m(\beta t + \psi_m)]$$

with

$$T_{m+1} = T_m/1.25$$

and

$$\sum_{m=1}^{m_{\max}} T_m = 1$$

In Eq. (20), A is the amplitude of the imposed disturbance, T_a and T_b are the arc-length values along the airfoil surface corresponding to the beginning and the end of the blowing/suction strip (values of arc length are measured starting from the leading edge), $z_{\max}$ is the spanwise extent of the computational region, β is the fundamental temporal frequency of the disturbance, and ϕ_l and ψ_m are uniformly distributed random numbers between 0 and 1. The parametric values used here are given next:

$$A = 0.6; \qquad T_a = 1.1(x/c = 0.158); \qquad T_b = 1.2(x/c = 0.258)$$
$$z_{\max}/c = 0.0863; \qquad l_{\max} = 11; \qquad m_{\max} = 5$$

The value of A was chosen to be relatively high, because the blowing/suction strip is in a region of the suction side where the flow is accelerating. It should be noted that if the local boundary layer edge

velocity were used in Eq. (20), instead of the inlet velocity u_∞, the corresponding value of A would be 0.25 (amplitude of imposed wall-normal velocity is 25% of local freestream velocity). The one-dimensional version of Eq. (20) (no variation in z) is similar to that of [17]. The two-dimensional version provided in Eq. (20) is identical to that of [18].

In [10], freestream turbulence with a prescribed turbulent intensity and integral length scale was numerically generated in the inlet region to obtain bypass transition on the flat plate. There, one of the objectives was to determine if the computed transition region would closely match the experimentally measured transition region if the numerically generated freestream turbulence had nearly the same intensity and length scale values as in the experiment. The spanwise dimension of the plate necessary to obtain the required longitudinal integral length scale was approximately three times the length scale itself. In the case of the airfoil, the experimentally measured length scale is approximately 0.8 in. for the case with grid-generated turbulence and much larger for the gridout case [16]. Even the smaller of the two (0.8 in.) would require a spanwise dimension approximately five times that used in the current airfoil computation. The fact that the high-resolution grid would need to extend all the way from the leading edge to the trailing edge on the suction side results in an additional factor of 2. The DNS would then require about 10 times as many grid points, thus resulting in a very expensive computation. In an effort to reduce computational costs in this first exploratory effort (HPT), we have resorted to blowing/suction. However, it should be noted that in the case of the airfoil, the adverse pressure gradient on the second half of the suction side of the airfoil is a desensitizing feature (with regard to transition location). The flow will tend to transition soon after the minimum pressure point ($x/c = 0.45$ in Fig. 3) for a range of freestream turbulence levels. Hence, the current approach (blowing/suction), which accomplishes essentially the same thing, can be expected to yield the transitional Stanton number distribution and velocity statistics that would be obtained in reality for a range of freestream intensity levels. At very high levels of freestream turbulence, transition will indeed move upstream of the minimum pressure point.

Inlet Boundary of the Inlet Zone

The flow at the inlet boundary of the inlet zone is subsonic. Four quantities must be specified at this boundary. The four used here are a Riemann invariant $R_1 = u + 2c/(\gamma - 1)$, the stagnation pressure, and the velocity components v and w. A second Riemann invariant $R_2 = u - 2c/(\gamma - 1)$ is extrapolated from the interior of the inlet zone to complete the system of equations required to uniquely define the dependent variables at the inlet. The resulting system of equations is given by

$$u_b - \frac{2c_b}{\gamma - 1} = u_2 - \frac{2c_2}{\gamma - 1}; \qquad u_b + \frac{2c_b}{\gamma - 1} = u_\infty + \frac{2c_\infty}{\gamma - 1}$$

$$v_b = 0; \qquad w_b = 0$$

$$p_b = P_\infty \left(1 + \frac{(\gamma - 1)}{2} \frac{(u_b^2 + v_b^2 + w_b^2)}{c_b^2}\right)^{-\gamma(\gamma - 1)} \tag{21}$$

In Eq. (21), c is the speed of sound, P is the stagnation pressure, and the subscripts b, 2, and ∞ refer to the inlet boundary, the grid point just downstream of this boundary, and the inlet reference conditions, respectively.

Exit Boundary of the Exit Zone

The flow at the exit boundary of the exit zone is subsonic. One flow quantity must be specified at this boundary. Here, the exit static pressure is specified, and the remaining variables are extrapolated from the interior. This boundary condition, together with the inlet boundary condition discussed previously, uniquely specifies the time-averaged mass flow through the system. However, it reflects pressure waves back into the system. To alleviate this problem, the grid is gradually coarsened in the x direction toward the exit boundary. This coarsening of the grid also has the advantage of nearly eliminating the wake before it encounters the exit boundary, thus permitting an inviscid exit boundary condition. The attenuation of the wake can be clearly seen in entropy contours presented later in the text.

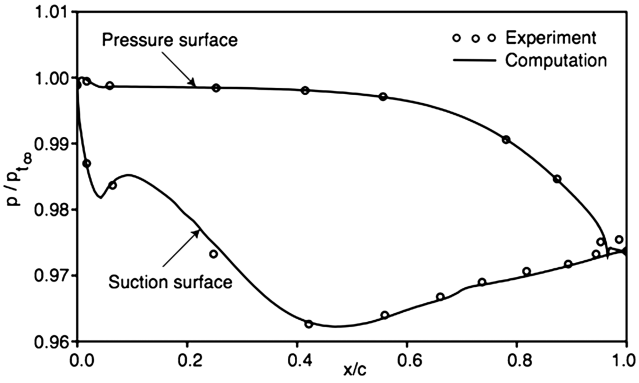

Fig. 3 Computed and experimental airfoil surface pressure distributions.

Periodic Boundary Conditions

Periodicity is imposed both in the spanwise direction and on the upper and lower boundaries in the y direction. Implementing periodicity in the spanwise direction for all the zones and on the upper and lower boundaries of the inlet and exit zones is straightforward. The portions of the upper and lower boundaries that correspond to the external grid require special treatment. This is because the grid points on the upper boundary are not at the same axial locations as those on the lower boundary. To overcome this problem, the outer boundary of the external grid is extrapolated (this, of course, can be a part of the grid generation process). Flow variables at the extrapolated points are obtained using interpolation and the periodicity condition. The implicit boundary condition in the η direction (required for the inversion in this direction) is identical to that used for zonal boundaries and is discussed next.

Zonal Boundary Conditions

The zonal boundaries that separate the various zones are treated using an interpolation procedure that is explicit at every substep (iteration) within a given time step, but which is implicit over the time step. To describe the procedure, we consider the outer boundary of the adjacent zone. This boundary corresponds to one of the constant η lines in the external grid, but the grid points of the two grids do not coincide. A cubic interpolation procedure (fourth-order accuracy) is used to interpolate the data (flow variables) on this curve from the external grid to the adjacent grid.

To integrate the equations of motion using the iterative-implicit scheme of Eq. (17), it is necessary to specify boundary conditions on the outer boundary of the adjacent zone to perform an inversion in the η direction. The boundary condition used here is given next:

$$Q_{zb}^{m+1} - Q_{zb}^{m} = 0 \tag{22}$$

where the subscript zb refers to the zonal boundary. After completing a substep in all the zones, the dependent variables on this zonal boundary are obtained by interpolating the data in the external zone. A similar postupdate correction is applied along all the zonal boundaries. One advantage of using this technique is that, during each substep, the computations within the various zones are uncoupled. It should be noted that Eq. (22) is not equivalent to

$$Q_{zb}^{n+1} - Q_{zb}^{n} = 0 \tag{23}$$

followed by a postupdate correction. Equation (22) permits $Q_{zb}^{n+1} - Q_{zb}^{n}$ to converge to its correct value when the iteration process is carried to convergence. Both time accuracy and spatial accuracy consistent with the order of interpolation and the order of accuracy of the integration scheme are maintained at the zonal boundary.

Equation (23), on the other hand, is an explicit boundary procedure and may affect the stability of the algorithm and require the use of smaller time steps. Additional details regarding the implicit zonal boundary condition can be found in [10,19].

Results

A low-speed turbine stator airfoil [16] was chosen for this study. It has undergone extensive testing to investigate rotor–stator interaction effects, as well as surface heat transfer at two levels of freestream turbulence. Figure 1 shows the midspan airfoil section. Here, we compute the flow using this airfoil cross section at all spanwise locations. Homogeneity is assumed in the spanwise direction, thus permitting the use of periodic boundary conditions at the spanwise extremes of the computational region. The spanwise extent of this region is about 2330 wall units based on the wall shear velocity in the turbulent flow at $x/c = 0.95$ on the suction side of the airfoil. The inlet Mach number for this case is 0.07, the unit Reynolds number based on inlet conditions is $40,300$/in., the inlet temperature is 518°R, and the ratio of the exit static pressure to the inlet total pressure is 0.9738.

In the experiment, transition was achieved by subjecting the airfoil to freestream turbulence. However, flow transition in this numerical investigation via DNS, was achieved by wall blowing and suction. The magnitude of blowing and suction was adjusted, such that transition occurred approximately at the same location on the airfoil as in one of the experiments. Only the suction side of the airfoil was subjected to wall blowing and suction. The pressure side of the airfoil was left undisturbed. This is because the current computation is modeled after the gridout case in the series of experiments [16] for which the turbulence-generating grid upstream of the stator was removed. The freestream turbulence level for this case is low (approximately 0.5% of freestream velocity). The measured heat transfer rate for this case indicates that the pressure side of the airfoil is essentially laminar. The grid used in the computation has the necessary resolution for DNS only on the suction side, thus reducing the computational cost by almost a factor of 2. The suction side exhibits laminar, transitional, and turbulent regions and hence possesses characteristics found in many complex flows.

The region in the vicinity of the trailing edge is well resolved. Interestingly, the wake comprises fluid from the laminar boundary layer on the pressure side and the turbulent boundary layer on the suction side. Hence, both types of boundary layers influence the shedding process. Although some flow visualization results of the trailing-edge region are presented here, a detailed discussion of the flow in this region will be provided in a separate paper.

Figure 1 shows the type of grid used for the computation in the vicinity of the airfoil. The grid lines moving away from the airfoil are perpendicular to the surface at the point of intersection. Velocity statistics are computed along these lines by first computing velocity components that are parallel and perpendicular to the airfoil surface (at the point of intersection of the respective grid line and the airfoil). These locally wall-normal and wall-tangential velocity components and the spanwise velocity component (v_N, v_T, and $v_s = w$, respectively) are used to generate the necessary velocity statistics. All the turbulence statistics presented here were obtained by averaging both in time and in the spanwise direction. The statistical samples were obtained over a period of 13 ms after the initial transients had subsided. This period corresponds to $720\delta^*/u_\infty$, where δ^* is the boundary layer displacement thickness at $x/c = 0.95$ and u_∞ is the inlet velocity, and it is also approximately the time required for a particle in the midpassage region to travel from the leading edge to the trailing edge twice. Almost all of the results presented here were obtained on the baseline grid (grid B). Results obtained on the fine grid are only provided for profiles of the normal intensities in the wall normal direction at $x/c = 0.95$. The sampling period used for the fine grid was approximately one-third of that used for the baseline grid. However, comparisons of intensity profiles obtained with both this smaller sampling period and the longer period of 13 ms (both on the baseline grid) showed that the smaller sampling period was adequate. This comparison is provided later in this section.

The iterative-implicit upwind-biased finite-difference method described earlier was used to compute the evolution of small-amplitude disturbances in a flat plate boundary layer in [10]. The computed results were compared with results from linear stability theory and the results of Gaster, and they were found to be in good agreement. The computations were performed with two, three, and four iterations per time step; the rms residual reductions obtained in the three cases were 12, 125, and 470, respectively. The solutions obtained in all three cases were very close. The DNS of transitional/turbulent flow on a flat plate that is reported in [10] was performed with three iterations per time step. An rms residual reduction of a factor of 15 was obtained in the finest grid used in the computation. Three iterations were also used in the present DNS, together with a time step ($\Delta t = 0.0225\delta^*/u_\infty$) that results in an rms residual reduction of about 15 in the adjacent grid.

Surface Pressure and Stanton Number Comparisons

Figure 3 shows the time-averaged pressure distribution on the surface of the airfoil normalized by the inlet total pressure and compared with experimental data [16]. The two distributions are in good agreement. Numerous computed surface pressure distributions that have been reported in the literature (obtained with the RANS equations) for turbine and compressor airfoils with a blunt trailing edge (circular, elliptic, and other shapes) exhibit a sharp decrease and subsequent rise in pressure very near the trailing edge. This behavior has also been observed in RANS simulations of the airfoil section used here. However, the current DNS and available experimental data only show a negligibly small dip on the pressure side near the trailing edge. Thus, this feature (sharp variations in pressure), in some of the cases reported in the literature, may be numerical in origin and caused by either inadequate grid resolution and/or the inadequacy of the turbulence model in the vicinity of the trailing edge. Small differences between the current computation and the experimental data seen in Fig. 3 are most probably because the experimental data are obtained in a three-dimensional rig with the attendant endwall boundary layers, passage vortices, and blade shape variation in the spanwise direction.

Figure 4 shows the time-averaged Stanton number distribution compared with experimental data. Here, the Stanton number is defined as in [16]:

$$St = q_w/[\rho_e U_e C_p(\theta_w - \theta_\infty)] \tag{24}$$

where ρ_e and U_e are the density and velocity, respectively, at the airfoil exit (in this case, the exit boundary of the exit zone). As mentioned earlier, the magnitude of blowing and suction near the leading edge, on the suction side of the airfoil, have been roughly adjusted so that the computed transitional flow is approximately in the same location as the experimental one. Hence, the proximity of the two transitions should not be interpreted as a close correspondence between freestream turbulence characteristics. In fact, freestream turbulence is absent in the computation. However, both the computation and the experiment show a rapid increase in the Stanton

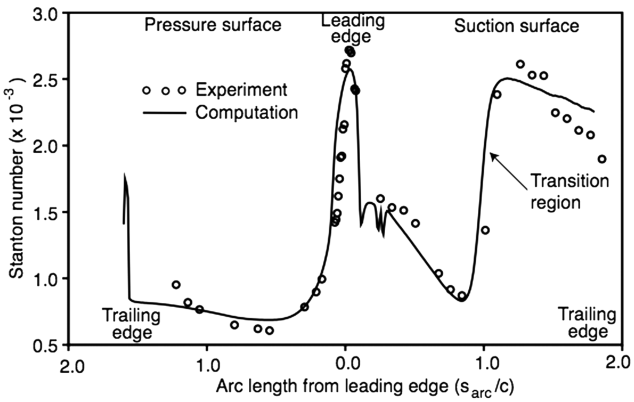

Fig. 4 Computed and experimental airfoil Stanton number distributions.

number in the transitional region on the suction side, followed by a very gradual decrease in the direction of the trailing edge. The two distributions agree reasonably well in the turbulent region downstream of transition. Computed Stanton number values near the leading edge and on the pressure side of the airfoil are close to experimental data and correspond to laminar flow. Once again, as in the case of the pressure distributions (Fig. 3), it must be noted that the experimental data represent a cross section of a fully three-dimensional flow.

Instantaneous Flowfield Visualizations

In the following figures, an instantaneous flowfield is investigated with the help of entropy and vorticity contours. The instant in time corresponds to the end of the 13 ms sampling period. A perspective view of the airfoil, focusing on the suction surface, is depicted in Fig. 5. The spanwise dimension (z) has been magnified by a factor of 5 to provide a better view of the flow structures. Instantaneous spanwise vorticity contours on the surface of the airfoil are depicted in this figure. The appearance of the vortical structures is quite abrupt. This location is slightly downstream of the pressure minimum on the suction side of the airfoil (Fig. 3). The flow transitions very soon after it encounters the adverse pressure gradient, following the pressure minimum, and then becomes turbulent further downstream. A careful examination of contours reveals higher magnitudes of vorticity in the transition region, followed by slightly lower values downstream. Velocity statistics (presented later in the text) also indicate higher levels of unsteadiness in the transition region. It should be noted that, because of the spanwise magnification, the vortical structures are also magnified by the same factor and are seen as being wider than in reality. The vorticity contours observed near the leading edge (crown of the airfoil) correspond to the imposed wall blowing and suction.

Figures 6 and 7 also show contours of spanwise vorticity. However, the viewing direction is normal to the airfoil surface at a particular location. This location was chosen to maximize the horizontal extent of Figs. 6 and 7. Hence, the viewing direction does not correspond to the negative y direction (Fig. 1). The spanwise dimension in these figures is not magnified, and hence the vortical structures are not distorted. Figure 6 shows contours in the transitional region, and Fig. 7 shows the corresponding contours in the turbulent region downstream. The appearance of the vortical structures in Fig. 6 is abrupt. Other instants in time show patches of intense vorticity immersed in the quiescent region upstream that are convected downstream and join the main body of vorticity, seen in Fig. 6. The boundary between the relatively quiescent and highly unsteady regions is complex and unsteady in nature. The more intense variation of vorticity in the transitional region, compared with the turbulent region, is evident in Figs. 6 and 7. Unlike Fig. 6, the vortical structures essentially fill the entire region in Fig. 7 and show a degree of pattern uniformity.

Instantaneous entropy contours at one spanwise location are shown in Fig. 8. End-stage transition and the development of the turbulent boundary layer downstream are evident here. Figure 9 shows entropy contours in the region of the trailing edge. Although grid resolution is adequate in the vicinity of the trailing edge (approximately 1 or 2 diameters downstream), the grid coarsens thereafter, causing the flow structures in the wake to dissipate. Unlike the downstream evolution of the wake, the near-wall (trailing edge) flow phenomena are believed to be accurately resolved. An interesting feature in Fig. 9 is that, although the shedding on the pressure side somewhat resembles laminar shedding with the corresponding roll up, shedding on the turbulent suction side of the airfoil is less obvious. In addition, on comparing Fig. 9 to laminar and RANS computations of trailing-edge flows (found in the literature and not included here), this turbulence seems to accelerate the breakup of the laminarlike vortices shed from the pressure side. The shedding phenomenon is of considerable interest in turbomachinery design, both from an acoustics perspective and in obtaining a better understanding of wake–blade interaction. Figure 10 shows spanwise vorticity contours in the trailing-edge region. The rapid dissipation of the turbulent flow structures because of the coarsening grid is evident

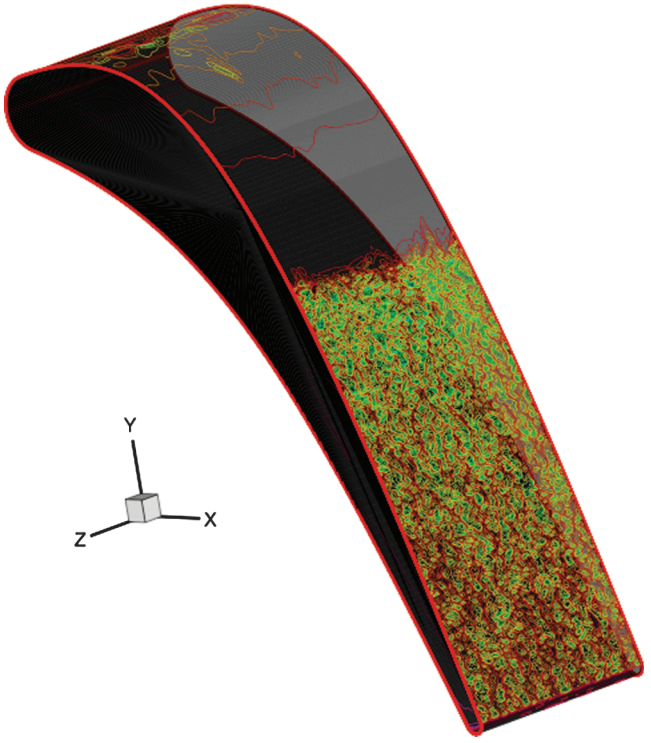

Fig. 5 Perspective view of airfoil showing surface instantaneous spanwise vorticity contours.

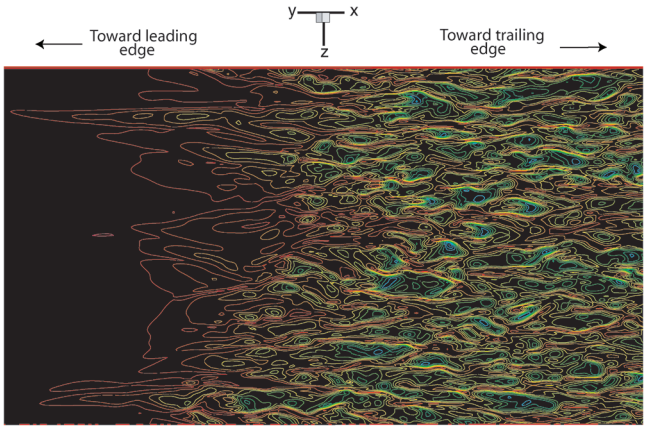

Fig. 6 Instantaneous spanwise vorticity contours on the airfoil (transitional region, top view).

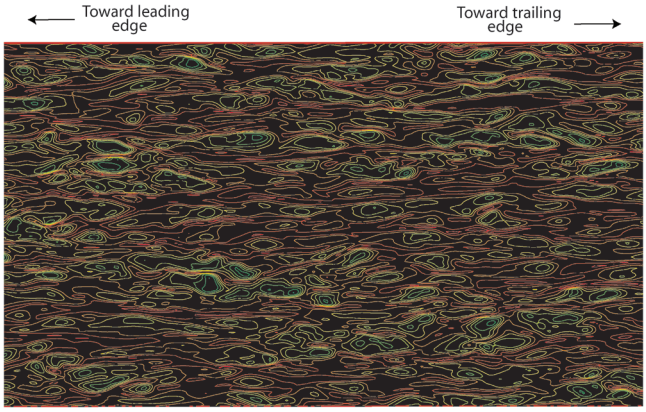

Fig. 7 Instantaneous spanwise vorticity contours on the airfoil (turbulent region, top view).

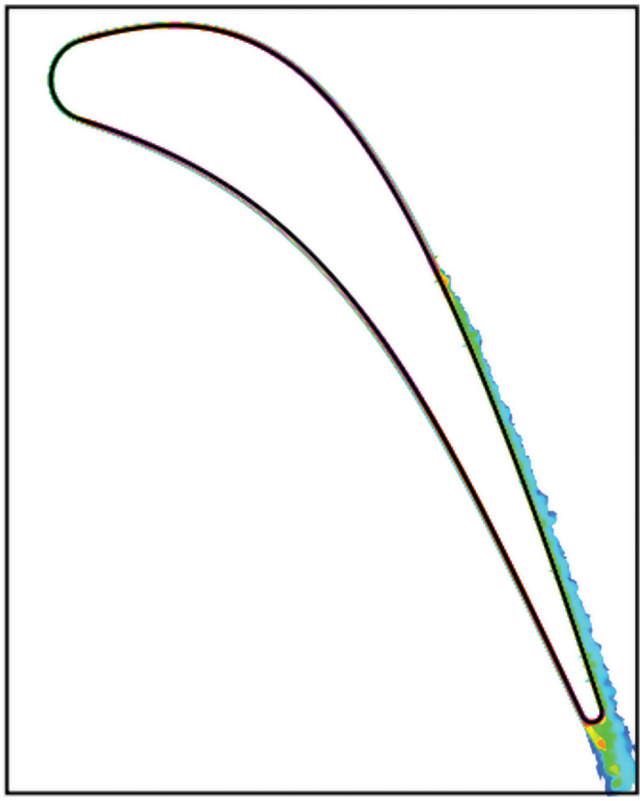

Fig. 8 Instantaneous entropy contours (full airfoil, side view).

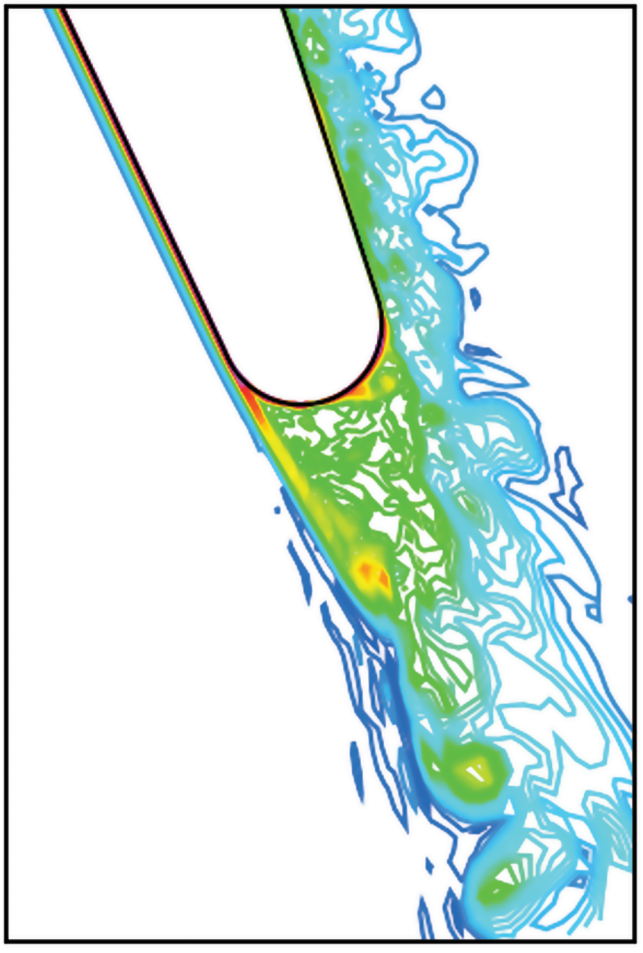

Fig. 9 Instantaneous entropy contours (airfoil trailing edge, side view).

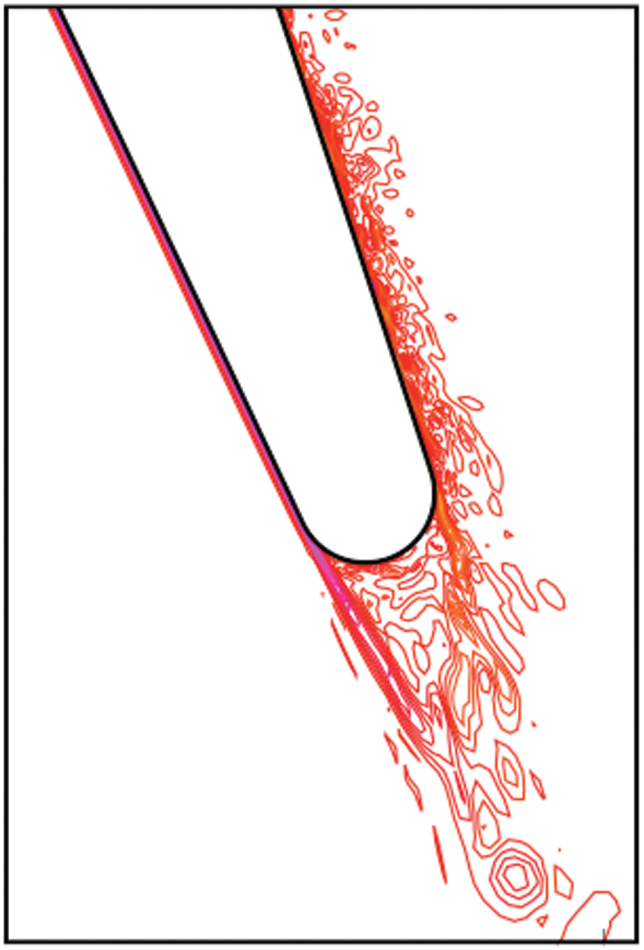

Fig. 10 Instantaneous spanwise vorticity contours (airfoil trailing edge, side view).

in this figure. DNS of rotor–stator interaction will require grids that yield accurate computations of wake evolution/convection.

Turbulence Statistics

In this subsection, we present some of the turbulence statistics obtained in the transitional and turbulent regions on the suction side of the airfoil. Figure 11 shows the growth of the boundary layer thickness as a function of the axial distance along the airfoil. The difference between the laminar and turbulent growth rates is evident. The transitional region extends between $x/c = 0.6$ and $x/c = 0.75$, depending on the statistic being considered (blowing and suction were applied in the region $0.158 < x/c < 0.258$). The thickness distribution shown in Fig. 11 is used later to normalize wall-normal distances.

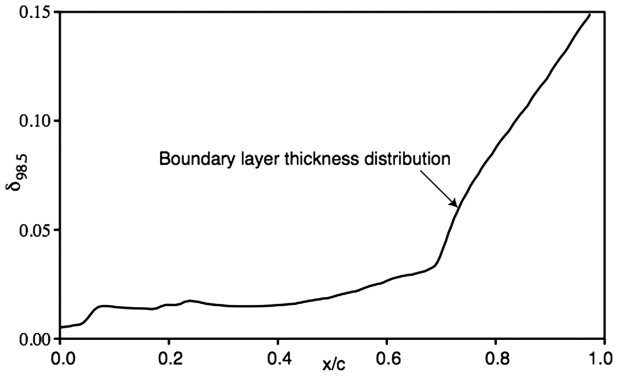

Fig. 11 Variation of boundary layer thickness on the suction side of the airfoil.

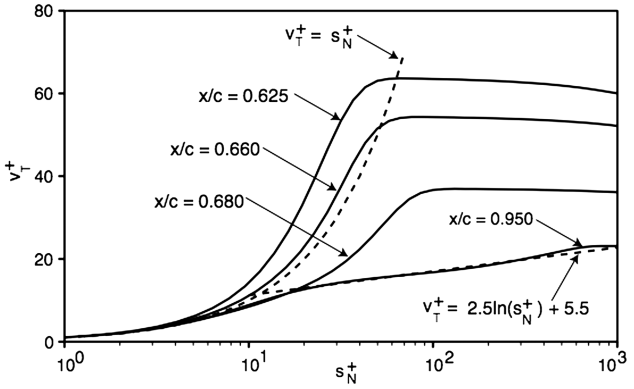

Fig. 12 Mean velocity profiles normalized by wall shear velocity at various locations on the airfoil.

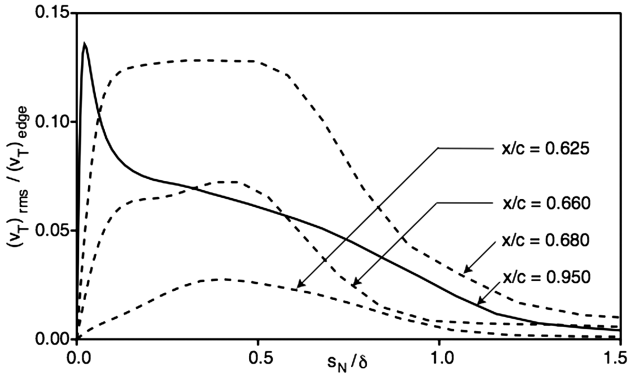

Fig. 14 Tangential component of turbulence intensity at various locations on the airfoil.

Figure 12 shows mean velocity profiles in the transitional and turbulent regions. The dashed lines represent the near-wall linear behavior ($v_T^+ = s_n^+$) and the log law ($v_T^+ = 2.5\,\ell_n(s_n^+) + 5.5$), where v_T^+ is the tangential component of velocity normalized by the wall shear velocity, and s_n^+ is the distance normal to the airfoil surface in wall coordinates. The first profile at $x/c = 0.625$ occurs just before the rapid increase in Stanton number. The next two profiles are from the transitional region ($x/c = 0.66$, 0.68), and the last one ($x/c = 0.95$) is in the turbulent region. The velocity profiles change rapidly in the transitional region and much more gradually thereafter; the evolution from transitional profiles to a turbulent profile is monotonic. The agreement with the linear profile and the log law at the station $x/c = 0.95$ is good.

The variation of the peak value of the turbulent intensity components as a function of the axial distance along the suction side of the airfoil is shown in Fig. 13. The wall shear velocity is used to normalize these peak intensity values. There is a sharp increase in intensity values in the transitional region ($0.6 < x/c < 0.7$), followed downstream by a sharp decrease in all of them. Subsequently ($x/c > 0.8$), the wall-tangential component shows very little change, whereas the wall-normal and spanwise components increase slowly in the axial direction. DNS of fully developed turbulence, on a flat plate with zero pressure gradient, are presented in [20]. Turbulence statistics are provided at Re_θ values of 300, 670, and 1410. The peak values of all three components of intensity increase slightly with increasing Re_θ, with the increase in the streamwise component between $Re_\theta = 600$ and $Re_\theta = 1410$ being almost negligible. The DNS results of [21], for a flat plate subjected to an adverse pressure gradient (discussed in greater detail later in the text) show the same trends but a larger increase in the peak intensity values with increasing Re_θ. The trends seen in Fig. 13, for the current situation with a mild adverse pressure gradient, are very similar.

Figure 14 shows the tangential component of the turbulent intensity in the transitional region ($x/c = 0.625$, 0.660, and 0.680) and the turbulent region ($x/c = 0.95$) as a function of the wall-normal distance (which is normalized by local boundary layer thickness). There is a very rapid increase in the peak value in the transition region, followed by a sharpening of the profile in the turbulent region. Figures 15 and 16 show the wall-normal and spanwise components of turbulent intensity at the same axial locations as in Fig. 14. The growth in peak value in the transition region, and the sharpening of the profile in the turbulent region, are similar to that in Fig. 14. The trends observed in Figs. 14–16 are very similar to those obtained in [10] for the case of bypass transition on a flat plate without a pressure gradient.

Figure 17 shows the turbulent intensities at $x/c = 0.95$, normalized by the local mean tangential velocity and plotted as a function of the distance normal to the wall (in wall coordinates). Experimental data obtained in a closed water channel [22] are also included in this figure. The tangential and spanwise components agree well with the experimental data. The limiting value at the wall of the tangential component is very nearly the same as the experimental value of 0.39. The normal component is lower than the experimental data near the

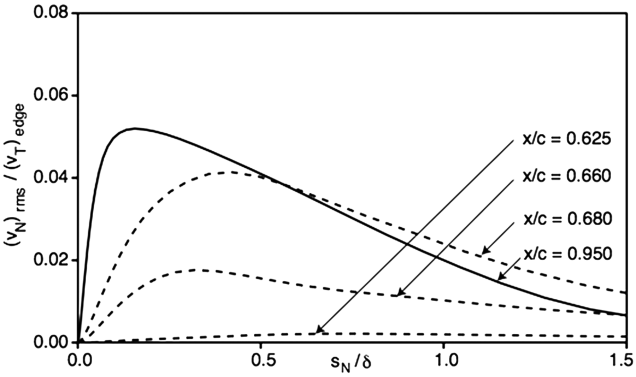

Fig. 15 Normal component of turbulence intensity at various locations on the airfoil.

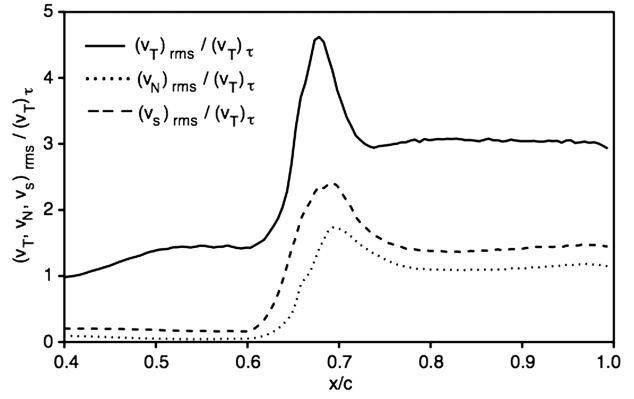

Fig. 13 Variation of peak turbulent intensities on the suction side of the airfoil.

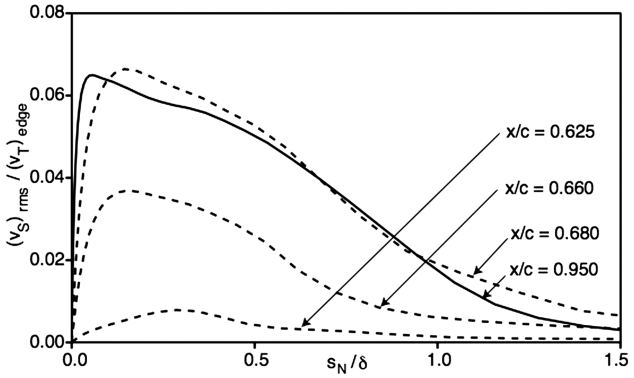

Fig. 16 Spanwise component of turbulence intensity at various locations on the airfoil.

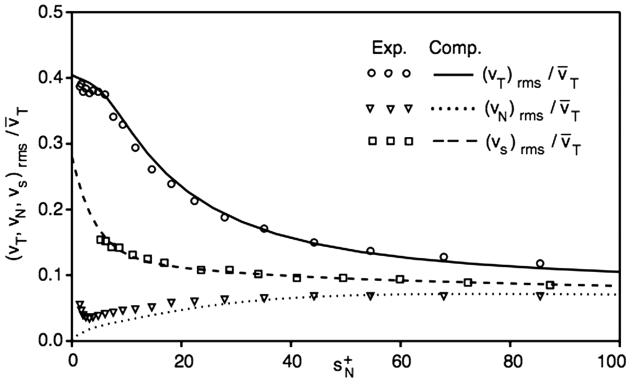

Fig. 17 Turbulence intensities, normalized by the local mean tangential velocity, at $x/c = 0.95$.

wall. The experimental data do not exhibit the expected linear behavior in the near-wall region. Instead, they increase as the wall is approached, thus indicating experimental error. The experimental wall-tangential and wall-normal data were obtained at $Re_\theta = 2420$ and the spanwise component at $Re_\theta = 1750$. The computed data are at $Re_\theta = 1780$. The comparison between the computation and the experiment is provided, even though the configurations are different (flat wall versus an airfoil boundary layer), because the airfoil exhibits very little curvature at $x/c = 0.95$ and because the adverse pressure gradient is mild.

Figure 18a shows the turbulent intensities at the same axial location. Here, the intensities are normalized by the wall shear velocity and are plotted as a function of the wall-normal distance (wall coordinates). The computed data are once again compared with the experimental data of [22]. There is good agreement between the two spanwise components and only a fair agreement between the wall-tangential and wall-normal components. The larger differences obtained for these two latter components are only partially because of the larger difference in Re_θ between the experiment and computation (there is close correspondence of Re_θ values for the experimental and computed spanwise component). Figure 18b shows the computed intensity profiles obtained on the fine grid. The computed tangential component is in better agreement with the experimental data with a peak value of 2.74 (the computed peak in Fig. 18 is 3.09). The other two components are slightly higher than before but still compare well with the experimental data. As mentioned earlier, the sampling period used for grid F is about one-third of the period used for the baseline grid. This was necessary to reduce computational cost. In Fig. 18c, the profiles computed on the baseline grid (Fig. 18a, 13 ms sampling period) are compared with profiles obtained on the same grid but with just 31% of the sampling period (4 ms). The proximity of the two sets of profiles demonstrates that the sampling period used for the grid F computation is adequate, and that the 13 ms sampling period used for all the grid B results, presented here, is a little more than adequate.

An earlier investigation of the evolution of a turbulent boundary layer on a flat plate, by Spalart and Watmuff [21], is of particular relevance here. They presented both experimental and computational results for a case with a unit Reynolds number of 428,000 per meter, based on inlet conditions. The streamwise extent (x) of the computational region is 1 m. The boundary layer is subjected to a favorable pressure gradient from 0.2 m, up to 0.6 m, and to an adverse pressure gradient from 0.6 m downstream. This pressure distribution is obtained by contouring the upper wall and is qualitatively similar to the suction side pressure distribution on the airfoil used here (Fig. 3). The pressure gradient parameter β ($\beta = \delta^*(\mathrm{d}p/\mathrm{d}x)/\tau_w$) ranges from $\beta = 0.0$ at $x = 0.63$ to $\beta = 2.0$ at $x = 1.0$. Both computational and experimental profiles of streamwise velocity, the three components of turbulent intensity, and the Reynolds shear stress are provided at the streamwise locations of $x = 0.4$, 0.6, 0.8, and 1.0.

The velocity statistics provided in [21] at $x = 0.6$ and $x = 0.8$ are of particular interest. The parameter β is close to 0 at $x = 0.6$ and is about 1.23 at $x = 0.8$. The corresponding values of Re_θ at these

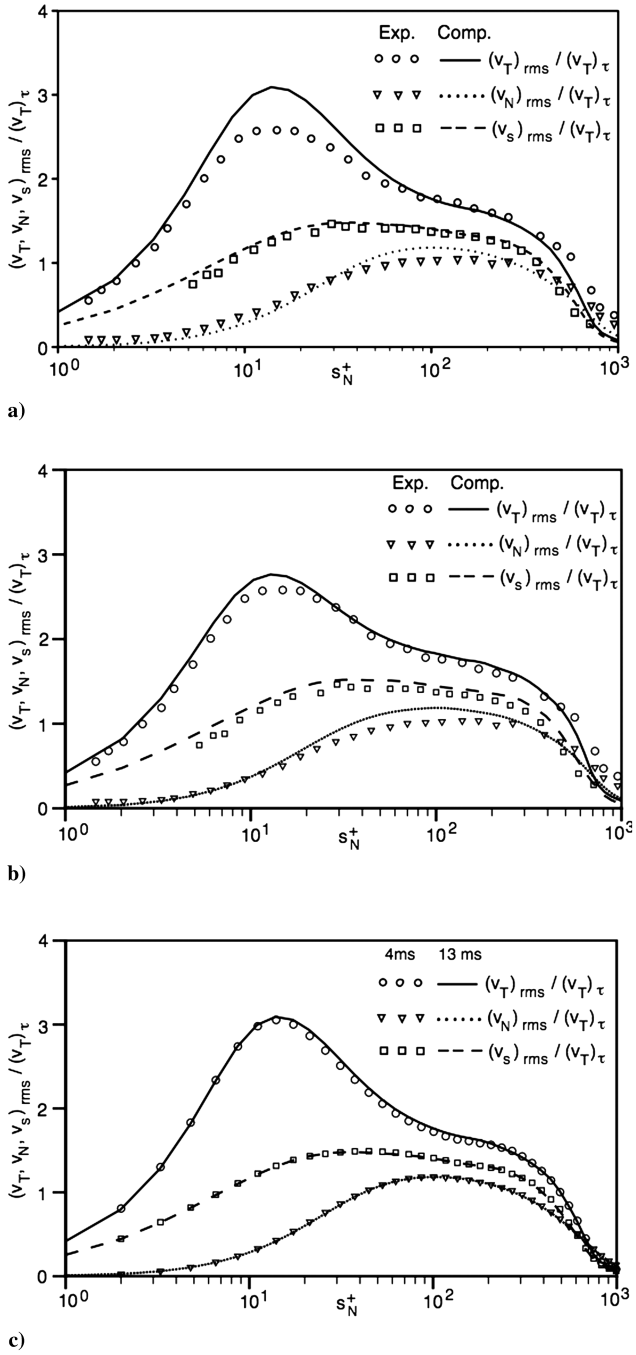

Fig. 18 Turbulence intensities normalized by local wall shear velocity a) at $x/c = 0.95$, b) at $x/c = 0.95$ (fine grid), and c) at $x/c = 0.95$ (baseline grid, 4 and 13 ms sampling periods).

streamwise locations are approximately 690 and 1120. The value of β in the current computation at $x/c = 0.95$ (turbulent flow regime) is about 0.27, and Re_θ is 1780. Because β plays a significant role in the evolution of the airfoil boundary layer (and because Re_θ for the airfoil and Re_θ at the location $x = 0.8$ are not far apart), it is reasonable to expect the velocity statistics obtained here to lie somewhere between those obtained at $x = 0.6$ and $x = 0.8$. A comparison very similar to those in Figs. 17 and 18, but with the computed results of [21], was performed. The turbulent intensities at $x/c = 0.95$, both normalized by the local mean tangential velocity (as in Fig. 17) and the local wall shear velocity (as in Fig. 18), for the most part fell right in between the data obtained at $x = 0.6$ and 0.8 in the region $s_n^+ < 100.0$. Thereafter, the results of [21] decay more rapidly than the present results. There are many other similarities between the data of [21] and the present simulation. For example, the peak values of the tangential (streamwise) component of turbulent intensity at the

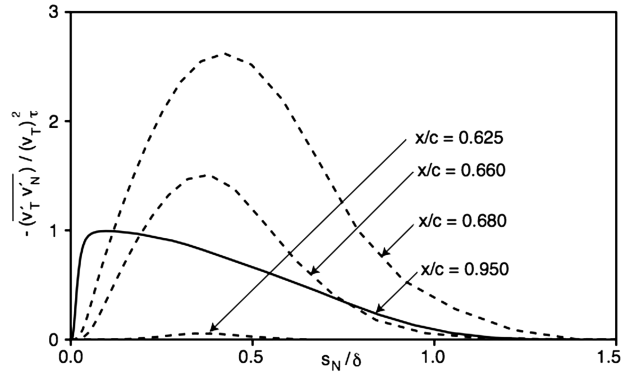

Fig. 19 Reynolds shear stress distributions at various locations on the airfoil.

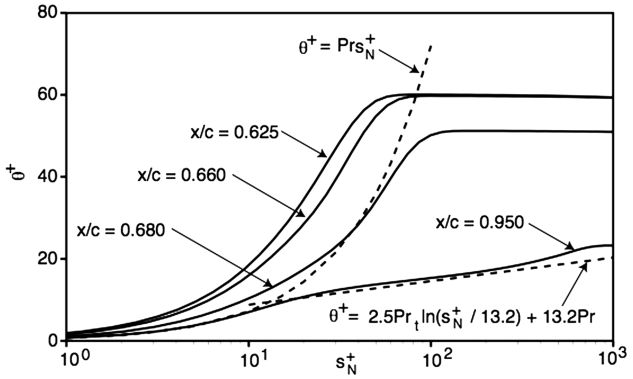

Fig. 21 Mean temperature profiles at various locations on the airfoil.

two locations, $x = 0.6$ and 0.8, are 13.3 and 12.3% of the boundary layer edge velocity, respectively. The current simulation yields a peak value of 13.4% at $x/c = 0.95$. Similar proximity in the data is seen in the other turbulent intensity components.

It is not our intent to make detailed comparisons with the data of [20–22]. The flow about the airfoil is different from those of [20–22]. The comparison between experimental and computational results in Figs. 17 and 18 and the preceding discussion of the data in [20,21] are provided to demonstrate that the turbulent intensities obtained here are reasonable. They are close to those obtained with similar Reynolds numbers and values of β. The author is not aware of previous experimental or computational turbulent intensity profiles for the airfoil used here.

Figure 19 shows Reynolds shear stress profiles at the same axial locations as in Figs. 14–16. Shear stress values in this figure are normalized by the square of the wall shear velocity and are plotted as a function of the wall-normal distance (normalized by the local boundary layer thickness). Shear stress values thus obtained are much higher in the transitional region than in the turbulent region downstream. Qualitatively, they follow the same trend as the turbulent intensity profiles. Figure 20 shows the Reynolds shear stress profile in the turbulent region ($x/c = 0.95$) plotted as a function of the wall-normal distance in wall coordinates. A comparison with the boundary layer data of [22] shows a fair agreement between the two data sets. The computed peak value is higher than seen in the experiment. Figure 20 also shows the computed results of [21], which were discussed earlier. The peak value of 0.96 obtained here lies between the computed values of [21] at $x = 0.6$ and 0.8 (estimated as 0.82 and 1.24, respectively). The peak obtained here is closer to the data at $x = 0.6$. This is probably because of the proximity of β values.

Figure 21 shows mean temperature profiles at the same axial locations as in Fig. 19. Temperature values in this figure are normalized by the friction temperature θ_τ, defined as

$$\theta_\tau = q_w/[\rho_w C_p (v_T)_\tau]$$

where $(v_T)_\tau$ is the wall shear velocity. The wall shear velocity at $x/c = 0.95$ was used to normalize all the profiles. This is because the rapid development of the momentum boundary layer in the transition region, and the consequent rapid increase in the wall shear velocity, results in a scrambling of the profiles, wherein profiles from downstream transition locations exhibit higher peak values. This phenomenon is also observed in the experimental results of [23] for the low freestream turbulence cases. Figure 21 also shows the near-wall approximation:

$$\theta^+ = Prs_n^+$$

and the logarithmic approximation from [24]:

$$\theta^+ = 13.2Pr + \frac{Pr_t}{\kappa}\ell_n\left(\frac{s_n^+}{13.2}\right)$$

The logarithmic profile was generated with $\kappa = 0.4$ and $Pr_t = 1.0$. The higher value of Pr_t was used instead of the conventional value of 0.9, because the computed DNS results here and in [25] (flat plate DNS with specified wall heat flux at $Re_\theta = 300$) show turbulent Prandtl number values close to 1.0 or even slightly higher in the region $10 \le s_n^+ \le 80$. The profiles in Fig. 21 show a monotonic transition from laminarlike to a turbulent profile. The computed profile at $x/c = 0.95$ clearly shows a logarithmic region, although it is slightly higher than the turbulent correlation of [24]. Choosing $s_n^+ = 14.5$ as the crossover point between the linear and logarithmic regions, instead of 13.2, yielded a significantly better agreement between the two curves, but it is not provided here. Although the profile at $x/c = 0.95$ corresponds closely to the approximation ($\theta^+ = Prs_n^+$ in the near-wall region), the other profiles are higher. In fact, all the computed profiles are very close to the linear profile in the near-wall region when normalized by the local friction temperature (computed using the local wall shear velocity).

The variation of rms temperature fluctuations in the wall-normal direction, plotted in wall coordinates and normalized by the local

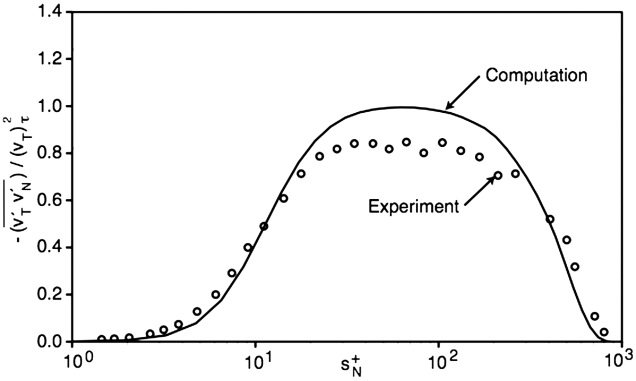

Fig. 20 Reynolds shear stress distribution, plotted in wall coordinates, at $x/c = 0.95$.

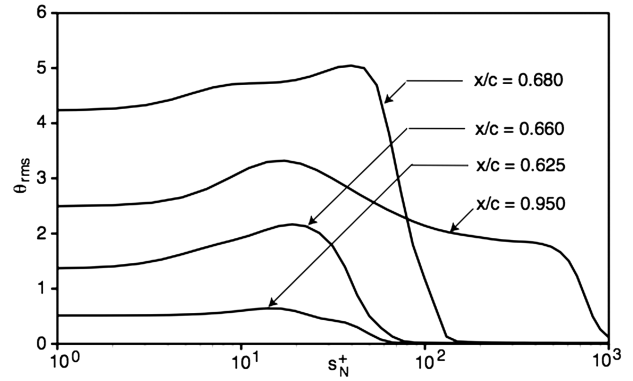

Fig. 22 RMS values of temperature fluctuations at various locations on the airfoil.

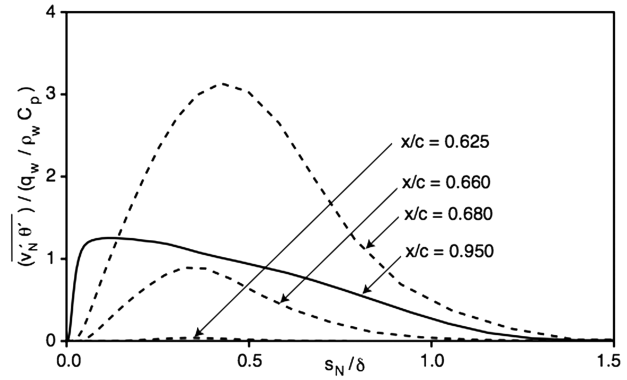

Fig. 23 Profiles of turbulent heat flux at various locations on the airfoil, normalized by $q_w/\rho_w C_p$.

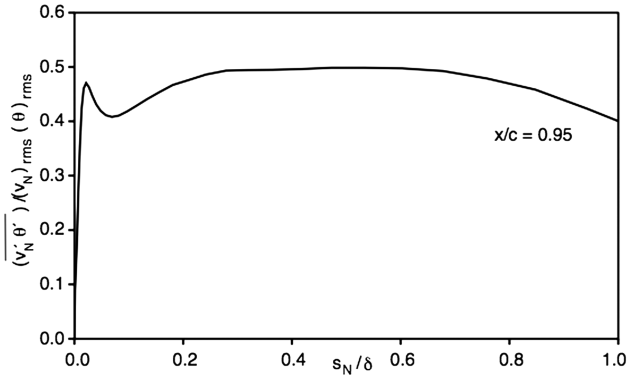

Fig. 24 Profile of turbulent heat flux at $x/c = 0.95$, normalized by $(v_n)_{\text{rms}}\theta_{\text{rms}}$.

friction temperature, are shown in Fig. 22. The axial locations of the profiles correspond to those in Fig. 21. There is a rapid increase in both the peak and wall values in the transitional region. The turbulent profile shows wall and peak values that are lower than obtained in the last transitional profile ($x/c = 0.68$) and, in wall coordinates, extends further ($s_n^+ \approx 1000$). These trends are very similar to those obtained in [26], in which DNS results for transition to turbulence on a heated flat plate are provided. The peak value in the turbulent region, obtained here (3.32), is higher than the range of data provided in [25] (between 2.4 and 2.8). The fine grid computation yielded a peak value of 3.07.

Figure 23 shows turbulent heat flux profiles at the same axial locations as in the previous figure. Here, the heat flux values have been normalized by $q_w/(\rho_w C_p)$. These profiles are very similar to the ones obtained for the Reynolds shear stress: a rapid increase through the transitional region, followed by a reduction in peak value and a sharpening of the profile in the turbulent region. The peak value observed at $x/c = 0.95$ is about 1.25. The peak value obtained in [26] is very close to 1.0, and the range provided in [25] extends between 0.75 and 0.85. Peak values above unity have been observed

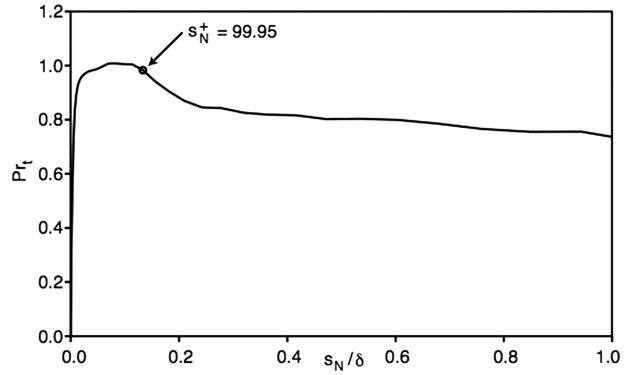

Fig. 25 Turbulent Prandtl number distribution at $x/c = 0.95$.

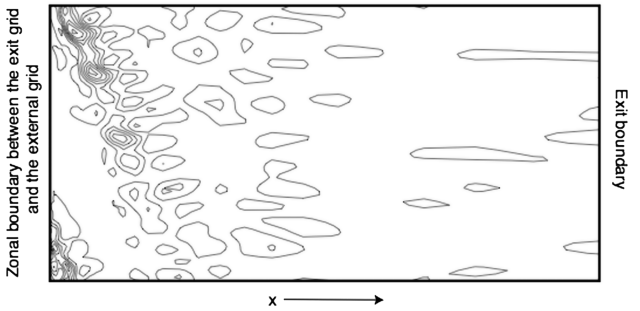

Fig. 26 Instantaneous entropy contours in the exit zone showing the numerical dissipation of the airfoil wake caused by the gradual coarsening of the grid in the axial direction.

in experiments in the posttransitional region [27]. The fine grid yielded a peak value at this location of 1.31. Figure 24 shows the profile at $x/c = 0.95$ but normalized by the local rms temperature fluctuations and the wall-normal component of the turbulent intensity (velocity). Except near the wall, the heat flux distribution is nearly constant at 0.5 in the boundary layer and is consistent with turbulent boundary layer data [23,27].

An important objective of a DNS of flow over a heated flat plate, presented in [26], was to investigate experimentally observed negative values of the turbulent heat flux in the near-wall region of the transitional boundary layer on a flat plate. Whereas some experiments report such unexpected behavior (for example, [23]), others do not [27]. Negative values of the turbulent heat flux were not observed in the corresponding DNS of [26]. In the present computation, negative values of this quantity were observed. The magnitude was very small (less than 0.4% of the peak value at $x/c = 0.95$ and not easily seen on the scale of Fig. 23). The region in which this was observed was at about $x/c = 0.63$. The size of the region was approximately four local boundary layer thicknesses in the streamwise direction. It is not clear if this phenomenon is real or simply an artifact of the wall blowing/suction procedure used to trip the boundary layer. A computation using numerically generated freestream turbulence may be required to resolve this issue. However, it must be emphasized that, from a practical point of view, because of the small magnitudes observed and because it is highly localized, this phenomenon may not be very relevant in the present case. Note that a normalization using the rms temperature fluctuations and the wall-normal component of the turbulent intensity (velocity), instead of the wall heat flux, magnifies the significance of this phenomenon, because the velocity statistic is itself very small in the near-wall region.

Figure 25 shows the turbulent Prandtl number distribution at $x/c = 0.95$. It is very close to unity in the near-wall region, dropping to zero at the wall. From $s_n/\delta > 0.14$ ($s_n^+ > 100.0$) onward, it gradually decreases to about 0.72 at the edge of the boundary layer. These results are consistent with the computed results of [25] and the experimental data of [27].

Figure 26 shows entropy contours in the exit zone. The wakes of two adjacent airfoils are observed near the left boundary. They gradually attenuate as they are convected downstream, because the grid coarsens in the axial direction from left to right. Only minor remnants of the wake remain at the exit boundary. As mentioned earlier, this permits the use of an inviscid exit boundary condition.

Conclusions

A DNS of transitional/turbulent flow on a low-speed turbine airfoil that is representative of an HPT vane is presented in this study. The nonconservative form of the Navier–Stokes equations for compressible flows is used for this simulation. The numerical method used to solve these equations is a high-order-accurate upwind-biased iterative-implicit finite-difference scheme and is an extension of a method used in earlier efforts in direct simulations of transition and turbulence on flat plates. The method and the associated natural boundary conditions are presented in the paper. In earlier investigations via DNS, the use of multiple zones aided in

distributing grid points appropriately and thus reduced the computational costs. Here, in addition to providing this utility, zoning of the computational grid facilitated the discretization of the more complex computational region. The zonal boundary conditions used here are also discussed in the paper. Clearly zoning will play an integral role in DNS of most practical aerodynamic configurations. The present effort has also resulted in a computer program that can be used fairly routinely for axial flow turbomachinery (single row) and makes efficient use of massively parallel computers. It is anticipated that DNS of turbomachinery airfoils will occur much more frequently in the next few years.

The results provided in the paper include time-averaged pressure and Stanton number distributions on the airfoil surface and turbulence statistics and flow visualizations in the transitional/turbulent regions. Comparisons with experimental and computational data obtained for flat plates and in channels are provided. A grid refinement study was conducted. The resolution provided in this computation was determined to be adequate for DNS in earlier simulations of channel flow. The refined grid provided statistics that were, for the most part, only slightly different than those obtained on the baseline grid. The velocity statistics in the turbulent region were found to agree fairly well with experimental data obtained for flat walls (both with and without pressure gradient). Even though the present case has attributes such as surface curvature and streamwise pressure gradient, overall, velocity and temperature statistics in the transitional and turbulent regions are in qualitative agreement with results obtained earlier via DNS for flat plates. The results indicate that the essential features of transition and turbulence have been captured in this case. They also indicate that the present finite-difference method can be used effectively and efficiently to perform DNS of turbulent/transitional flow.

References

[1] Wu, X., and Durbin, P. A., "Evidence of Longitudinal Vortices Evolved from Distorted Wakes in a Turbine Passage," *Journal of Fluid Mechanics*, Vol. 446, Nov. 2001, pp. 199–228.

[2] Rogers, M. M., "The Evolution of Strained Turbulent Plane Wakes," *Journal of Fluid Mechanics*, Vol. 463, July 2002, pp. 53–120. doi:10.1017/S0022112002008686

[3] Wissink, J. G., "DNS of Separating, Low Reynolds Number Flow in a Turbine Cascade with Incoming Wakes," *International Journal of Heat and Fluid Flow*, Vol. 24, No. 3, Aug. 2003, 626–635. doi:10.1016/S0142-727X(03)00056-0

[4] Wissink, J. G., Rodi, W., and Hodson, H. P., "The Influence of Disturbances Carried by Periodically Incoming Wakes on the Separating Flow Around a Turbine Blade," *International Journal of Heat and Fluid Flow*, Vol. 27, No. 4, Aug. 2006, 721–729. doi:10.1016/j.ijheatfluidflow.2006.02.016

[5] Wissink, J. G., and Rodi, W., "Direct Numerical Simulation of Flow and Heat Transfer in a Turbine Cascade with Incoming Wakes," *Journal of Fluid Mechanics*, Vol. 569, Dec. 2006, pp. 209–247. doi:10.1017/S002211200600262X

[6] Liu, X., and Rodi, W., "Velocity Measurements in Wake-Induced Unsteady Flow in a Linear Turbine Cascade," *Experiments in Fluids*, Vol. 17, Nos. 1–2, June 1994, pp. 45–58. doi:10.1007/BF02412803

[7] Liu, X., and Rodi, W., "Surface Pressure and Heat Transfer Measurements in a Turbine Cascade with Unsteady Oncoming Wakes," *Experiments in Fluids*, Vol. 17, No. 3, July 1994, pp. 171–178. doi:10.1007/BF00190914

[8] Zaki, T., Durbin, P. A., Wissink, J. G., and Rodi, W., "Direct Numerical Simulation of By-Pass and Separation Induced Transition in a Linear Compressor Cascade," *ASME Turbo Expo 2006: Power for Land, Sea, and Air*, American Society of Mechanical Engineers Paper GT-2006-90885, Fairfield, NJ, May 2006.

[9] Rai, M. M., and Moin, P., "Direct Simulations of Turbulent Flow Using Finite-Difference Schemes," *Journal of Computational Physics*, Vol. 96, No. 1, Sept. 1991, pp. 15–53. doi:10.1016/0021-9991(91)90264-L

[10] Rai, M. M., and Moin, P., "Direct Numerical Simulation of Transition and Turbulence in Spatially Evolving Boundary Layer," *Journal of Computational Physics*, Vol. 109, No. 2, Dec. 1993, pp. 169–192. doi:10.1006/jcph.1993.1210

[11] Kim, J., and Moin, P., "Application of a Fractional Step Method to Incompressible Navier–Stokes Equations," *Journal of Computational Physics*, Vol. 59, No. 2, 1985, pp. 308–323. doi:10.1016/0021-9991(85)90148-2

[12] Chakravarthy, S. R., Anderson, D. A., and Salas, M., "The Split Coefficient Matrix Method for Hyperbolic Systems of Gas Dynamic Equations," AIAA Paper 80-0268, Pasadena, CA, 1980.

[13] Rai, M. M., and Chakravarthy, S. R., "An Implicit Form for the Osher Upwind Scheme," *AIAA Journal*, Vol. 24, No. 5, May 1986, pp. 735–743. doi:10.2514/3.9340

[14] Rizetta, D. P., Visbal, M. R., and Morgan, P. E., "A High-Order Accurate Compact Finite-Difference Scheme for Large-Eddy Simulations of Active Flow Control," *Progress in Aerospace Sciences*, Vol. 44, No. 6, Aug. 2008, pp. 397–426. doi:10.1016/j.paerosci.2008.06.003

[15] Gordnier, R. E., and Visbal, M. R., "Numerical Simulation of Delta-Wing Roll," 31st Aerospace Sciences Meeting, AIAA Paper 1993-554, 1993.

[16] Dring, R. P., Blair, M. F., Joslyn, H. D., Power, G. D., and Verdon, J. M., "The Effects of Inlet Turbulence and Rotor/Stator Interactions on the Aerodynamics and Heat Transfer of a Large-Scale Rotating Turbine Model," NASA CR-4079, 1987.

[17] Fasel, H. F., Rist, U., and Konzelman, U., "Numerical Investigation of the Three-Dimensional Development in Boundary-Layer Transition," *AIAA Journal*, Vol. 28, No. 1, Jan. 1990, pp. 29–37. doi:10.2514/3.10349

[18] Rai, M. M., Gatski, T. B., and Erlebacher, G., "Direct Numerical Simulation of Spatially Evolving Compressible Turbulent Boundary Layers," 33rd Aerospace Sciences Meeting, AIAA Paper No. 95-0583, Jan. 1995.

[19] Rai, M. M., "An Implicit, Conservative, Zonal-Boundary Scheme for Euler Equation Calculations," *Computers and Fluids*, Vol. 14, No. 3, 1986, pp. 295–319. doi:10.1016/0045-7930(86)90027-7

[20] Spalart, P. R., "Direct Simulation of a Turbulent Boundary Layer Up To $Re_\theta = 1410$," *Journal of Fluid Mechanics*, Vol. 187, Feb. 1988, pp. 61–98. doi:10.1017/S0022112088000345

[21] Spalart, P. R., and Watmuff, J. H., "Experimental and Numerical Study of a Turbulent Boundary Layer with Pressure Gradients," *Journal of Fluid Mechanics*, Vol. 249, April 1993, pp. 337–371. doi:10.1017/S002211209300120X

[22] Karlsson, R. I., and Johansson, T. G., "LDV Measurements of Higher-Order Moments of Velocity Fluctuations in a Turbulent Boundary Layer," *Proceedings of the 3rd International Symposium on Applications of Laser Anemometry to Fluid Mechanics*, Instituto Superior Tecnico, Lisbon, 1988, pp. 273–289.

[23] Sohn, K. H., and Reshotko, E., "Experimental Study of Boundary Layer Transition with Elevated Free-Stream Turbulence on a Heated Flat Plate," NASA CR-187068, Feb. 1991.

[24] Kays, W., Crawford, M., and Weigand, B., "Convective Heat and Mass Transfer," 4th ed., McGraw–Hill, New York, 2005.

[25] Hong, H., Choi, H., and Lee, J. S., "Direct Numerical Simulation of Turbulent Thermal Boundary Layers," *Physics of Fluids*, Vol. 12, No. 10, Oct. 2001, pp. 2555–2568. doi:10.1063/1.1287912

[26] Madavan, N. K., and Rai, M. M., "Direct Numerical Simulation of Boundary Layer Transition, on a Heated Flat Plate with Elevated Free-stream Turbulence," 33rd Aerospace Sciences Meeting, AIAA Paper 95-0771, Jan. 1995.

[27] Kim, J., and Simon, T. W., "Freestream Turbulence and Concave Curvature Effects on Heated Transitional Boundary Layers," NASA CR-187150, 1991.

J. Oefelein
Associate Editor